OPEN ACCESS
IOP Publishing
Journal of Physics D: Applied Physics
J. Phys. D: Appl. Phys. **55** (2022) 475203 (18pp)
https://doi.org/10.1088/1361-6463/ac9538

Plasma breakdown in bubbles passing between two pin electrodes

Naveen Pillai[1], Nicholas L Sponsel[1], J T Mast[1], Mark J Kushner[2], Igor A Bolotnov[1] and Katharina Stapelmann[1,*]

[1] Department of Nuclear Engineering, North Carolina State University, Raleigh, NC 27695, United States of America
[2] Electrical Engineering and Computer Sciences Department, University of Michigan, Ann Arbor, MI 48109-2122, United States of America

E-mail: kstapel@ncsu.edu

Received 1 August 2022, revised 13 September 2022
Accepted for publication 27 September 2022
Published 7 October 2022

Abstract

The ignition of plasmas in liquids has applications from medical instrumentation to manipulation of liquid chemistry. Formation of plasmas directly in a liquid often requires prohibitively large voltages to initiate breakdown. Producing plasma streamers in bubbles submerged in a liquid with higher permittivity can significantly lower the voltage needed to initiate a discharge by reducing the electric field required to produce breakdown. The proximity of the bubble to the electrodes and the shape of the bubbles play critical roles in the manner in which the plasma is produced in, and propagates through, the bubble. In this paper, we discuss results from a three-dimensional direct numerical simulation (DNS) used to investigate the shapes of bubbles formed by injection of air into water. Comparisons are made to results from a companion experiment. A two-dimensional plasma hydrodynamics model was then used to capture the plasma streamer propagation in the bubble using a static bubble geometry generated by the DNS The simulations showed two different modes for streamer formation depending on the bubble shape. In an elliptical bubble, a short electron avalanche triggered a surface ionization wave (SIWs) resulting in plasma propagating along the surface of the bubble. In a circular bubble, an electron avalanche first traveled through the middle of the bubble before two SIWs began to propagate from the point closest to the grounded electrode where a volumetric streamer intersected the surface. In an elliptical bubble approaching a powered electrode in a pin-to-pin configuration, we experimentally observed streamer behavior that qualitatively corresponds with computational results. Optical emission captured over the lifetime of the streamer curve along the path of deformed bubbles, suggesting propagation of the streamer along the liquid/gas boundary interface. Plasma generation supported by the local field enhancement of the deformed bubble surface boundaries is a mechanism that is likely responsible for initiating streamer formation.

Keywords: plasma, low-temperature, DNS, bubbles, simulation

(Some figures may appear in colour only in the online journal)

* Author to whom any correspondence should be addressed.

1. Introduction

The aim of plasma treated water (PTW) is to introduce reactive oxygen and nitrogen species (RONSs) to a bulk liquid for medical [1], agricultural [2], and other uses [3]. The species densities and mole fractions of long-lived RONS in a liquid are highly dependent on feed gas, humidity and discharge regime (spark or glow), while significantly varying between different devices [4]. This variability grants the user some ability to tailor discharge conditions to select for the desired combination of RONS. However, scaling plasma sources to treat increasing volumes of liquid continues to be a challenge.

Solvation is a dominant mechanism for transporting plasma produced RONS into the liquid whether the liquid is in direct contact with the plasma or the liquid is treated by the effluent of a remote plasma. Sustaining a plasma in bubbles in the liquid increases the surface-area-to-volume ratio of the plasma-liquid interface, thereby increasing the transport of RONS from the bulk plasma into the liquid. Bubbles also confine plasma produced effluent to interacting with the bulk liquid for times determined by the convective transport from discharge position to the liquid surface. Modification of the plasma-to-liquid transport time can then be adjusted by bubble size and liquid depth. Plasmas in bubbles, by virtue of the liquid surrounding the plasma, provide a single unique destination, the liquid surface, for species diffusing out of the plasma.

The shape of the bubble in which the plasma is sustained is also an important consideration. Assuming that voltage is applied by electrodes external to the bubble, ellipsoidal bubbles produce greater electric field enhancement at the boundary between the higher permittivity liquid and gaseous bubble than that with equivalent spherical bubbles [5]. The local electric field enhancement impacts the manner in which plasma breakdown occurs across or along the surface of the liquid/gas interface. To understand and predict plasma breakdown properties in bubbles using external electrodes, the shape and evolution of the bubble are important as the rising bubble approaches, and in some cases collides with, an electrode.

Sophisticated three-dimensional (3D) models coupling computational fluid dynamics (CFDs), electromagnetics, plasma-surface interactions, and mixture-dependent thermodynamics have been developed for thermal plasmas [6–8]. CFDs with fluid dynamic-thermal-electromagnetic coupling have mostly been applied for high-power plasma discharges which are or are close to local thermal equilibrium [9]. Examples include the CFD simulation of radio-frequency plasma torches or the 3D simulation of electric welding [10, 11]. In many plasma-liquid interface models, the liquid is represented as a thin layer [12–16], or as droplets [17]. Typically, non-thermal, non-equilibrium plasmas are described by decoupled approaches, which works well in most cases [18–20]. However, in the case of plasma-water interactions with a non-thermal, non-equilibrium atmospheric pressure plasma, as described in this work, a multi-physics framework is necessary to provide a form of coupling between CFD and the plasma simulations.

In a practical implementation producing large volumes of PTW using the plasma-in-bubbles method, it is unlikely that a single bubble will be statically confined between two electrodes. It is more likely that a stream of bubbles will be produced at a deeper depth than the electrodes, with the bubbles then rising to intersect with the stationary electrodes. The challenge with simulating these conditions is resolving the physics when multiple bubbles intersect the electrodes. There have been several investigations of bubbles interacting with flat solid surfaces [21–24]. A review is available of bubbles interacting with particles [25] (i.e. solids much smaller than the bubble). However, there have been few investigations of bubbles hitting obstacles that might perturb their shape [26, 27]. Alizadeh *et al* [26] assessed the relative size of the bubbles before and after impact. Chen *et al* [27] investigated the relationship between the projection area ($A_p/\pi R^2$)—in that case, the area of the bubble in the plane perpendicular to bubble travel (and thus gravitation force)—and the bubble rise velocity ($v/\sqrt{2gR}$) during the collision with the obstacle. In both studies, the authors note that when increasing the obstacle, the hindrance to the shape of the bubble and time it takes for the bubble to recover are increased.

In this paper, we discuss results from a computational investigation of rising air bubbles in water interacting with a pair of pin-to-pin electrodes, the resulting plasma production inside the bubbles, and experimental assessment of bubble variations, along with qualitative comparison of plasma behavior at the liquid/gas interface. The fluid dynamic influences on millisecond timescales between multiple bubbles and solid electrodes are addressed using a five-nozzle capillary gas feed. Data generated both computationally and experimentally for five-nozzle instances are used to determine bubble shape, size, motion, and collisional deformations with electrodes. Electric dynamics on nanosecond timescales between a single bubble and the electrode gap are addressed by modeling a single, static bubble computationally; and a single-nozzle capillary gas feed experimentally. The domain for modeling the plasma production is shown in figure 1.

The bubble shapes, trajectories, and collisional interactions with electrodes were computed with 3D direct numerical simulations (DNSs), which is a high resolution CFD without turbulence modeling. The bubble shapes were then transferred to a two-dimensional (2D) plasma hydrodynamics model with which breakdown and streamer propagation were predicted. The models used in this investigation are described in section 2.

Experimental imaging of rising bubbles flowing between, and interacting with, the pin-to-pin electrodes was performed to validate bubble shapes and sizes observed through DNS. The target of the investigation is the effect that deformed gas/liquid boundaries have on plasma propagation across the boundary surface or through the gas phase of the bubbles. As such, the aim of the experiment was to capture discharge optical emission from a region in a bubble's progression through a bulk liquid at which the bubble interface is maximally deformed. The bubble boundary was held static in the plasma model to computationally determine streamer propagation across the domain. To compare to experimental results, capturing optical emission experimentally requires recording discharge events across several bubbles. In the case

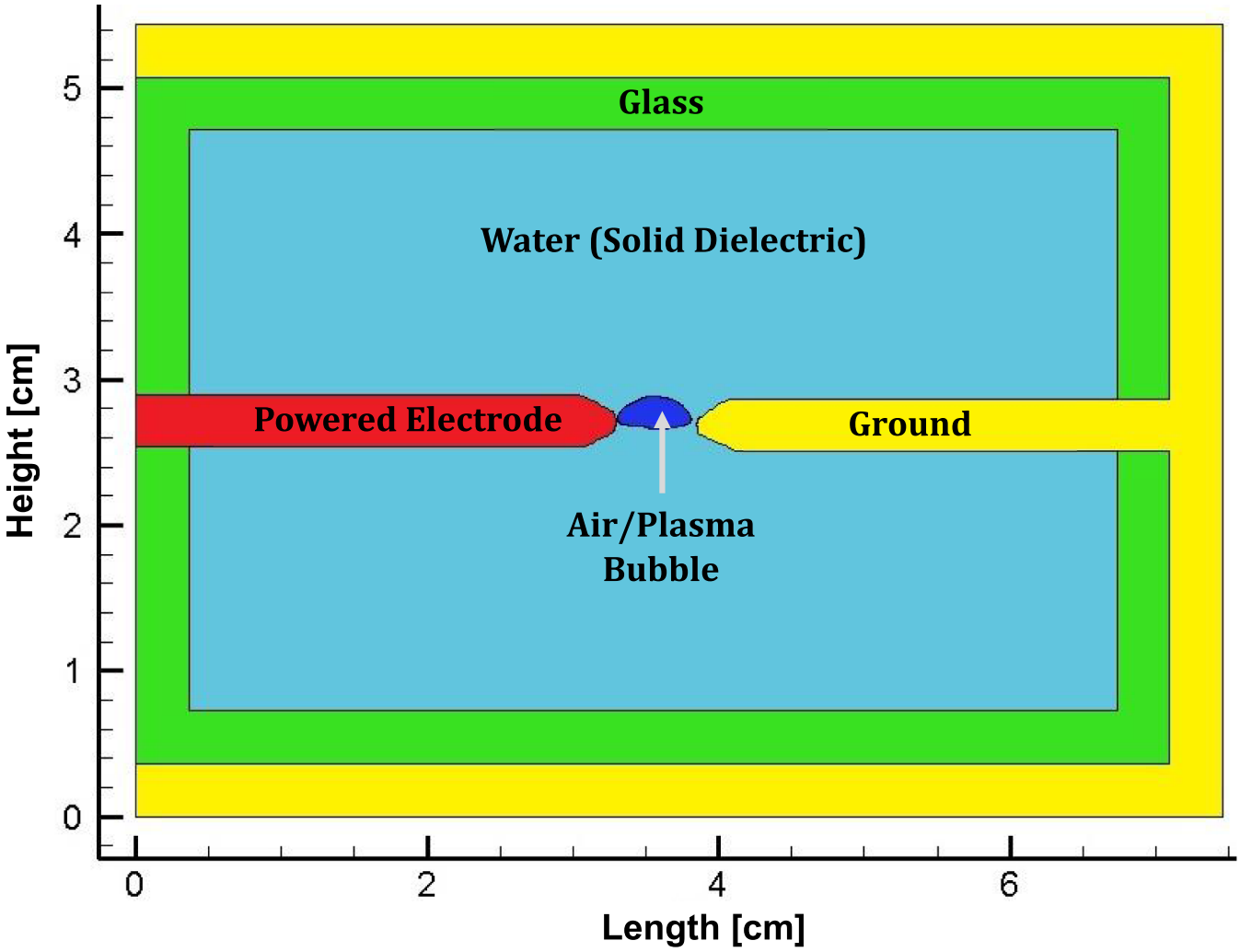

Figure 1. Assignment of materials for pin-to-pin plasma simulations in *nonPDPSIM*. The copper electrodes have diameters of 3.2 mm, and the diameter of the tips is 0.8 mm. The tips of the electrodes are spaced 5 mm apart. The ground electrode is extended to the top to provide a voltage boundary condition for the simulation. The water is treated as a lossy solid dielectric in the plasma simulations.

of the deformed bubbles targeted in this experiment, reproducibility of a single bubble shape and position is difficult, and a statistical approach must be utilized. Long exposure images were implemented to capture the qualitative behavior of the plasma produced in the bubbles over the lifetime of a few plasma discharge events.

We found that discharges occur more frequently when a bubble collides with one of the electrodes, which is common due to the serpentine flow behavior of the rising bubbles. Imaging was performed under dark conditions to capture only the light emitted from electric breakdown. However, the location of the bubble boundaries was found by utilizing a large image set of bubble positions and shapes taken with a backlight capturing the silhouette of bubbles and electrodes (see section 3) [28]. Over the entirety of the discharge, the emission curved in a manner that suggests surface streamers propagated across the deformed interface of the bubble. This observation compliments the computational results for deformed, non-spherical bubbles in which plasma propagation carries forward in time with interface-bound propagation (see section 4.3). Due to discrepancies between the 2D model which uses projections of the bubble shape and the 3D nature of the bubbles, discharge that appears over a straight path cannot necessarily be interpreted with confidence as a volumetric discharge through the gas. That said, in the case of the images collected from collisional, deformed bubbles, distinctly curved discharge emission is the predominant feature.

2. Computational methods

In this section, we describe the two models used for simulation of the rising bubbles and plasma production in the bubbles. The dynamics of the rising bubbles were addressed using the DNS code PHASTA [29, 30]. The plasma dynamics were addressed with the *nonPDPSIM* modeling platform [31].

2.1. Overview of DNS solver—PHASTA

The fluid dynamics simulations were performed using a two-phase flow solver—PHASTA [29, 30]. PHASTA is a Parallel,

Hierarchic, higher-order, Adaptive, Stabilized, Transient Analysis flow solver that is able to simulate incompressible flows in 3Ds on an unstructured grid using the finite element method.

PHASTA is an open-source code that has been developed by several research groups into specialty applications. PHASTA is one of the first codes developed and used for large eddy simulation on unstructured grids [32]. The functionality with unstructured grids continues to be one of its main strengths, as it has the capability to take in a variety of element shapes in the input mesh, including tetrahedrons that are typically used in the bulk region, and prisms that are very useful to create boundary layers from walls. These boundary layers can either be of uniform length or can systematically grow outward from the walls. This assures that layers of elements are parallel to the wall which is helpful when implementing wall boundary conditions that strongly affect the fluid flow or resolving interesting phenomena that occur near walls. While PHASTA was originally developed for single-phase flow, it has since been expanded to be able to simulate two-phase flow between any two immiscible fluids. This was done using the level set method developed by Sussman *et al* [33] and Sethian [34]. With the level set method, the Navier–Stokes equations are integrated for one fluid and the properties of the fluid are blended at the interface using a smoothed Heaviside function. Another set of equations are solved to keep track of the interface. While there are other interface tracking methods that use the single fluid approach—namely front tracking and the volume of fluid method—the level set method is thought to be more accurate at resolving highly curved and deformable interfaces, especially when multiple interfaces are in close proximity to each other [35].

Both liquid and gas bubbles were treated as incompressible fluids. PHASTA was used to solve the incompressible Navier–Stokes equations,

$$\nabla \cdot \underline{u} = 0 \tag{1}$$

$$\rho\left(\frac{\partial \underline{u}}{\partial t} + \underline{u}\cdot\nabla\underline{u}\right) = -\nabla \underline{P} + \nabla\cdot\underline{\underline{\tau}} + \underline{f} = 0$$

$$\underline{\underline{\tau}} = \mu\left(\nabla\underline{u} + \nabla\underline{u}^T\right) \tag{2}$$

where $\underline{u}$ is the velocity field, ρ is the mass density, t is time, $\underline{P}$ is the static pressure field, $\underline{\underline{\tau}}$ is the viscous stress tensor, $\underline{f}$ denotes the body forces (gravity and surface tension [36]), and μ is the viscosity. The interface between the two fluids was tracked by a scalar (ϕ) that is advected along with the fluid,

$$\frac{\partial \phi}{\partial t} + \underline{u}\cdot\nabla\phi = 0 \tag{3}$$

where negative values of the scalar (ϕ) signify the gas phase, and positive values signify the liquid phase, with the interface represented at $\phi = 0$. Since a discontinuity in fluid properties would be difficult for the solver to resolve, the fluid properties (density, viscosity and surface tension) are ramped across the interface according to a smoothed Heaviside function (figure 2) and with a fixed user-defined interface half-thickness, ϵ [33];

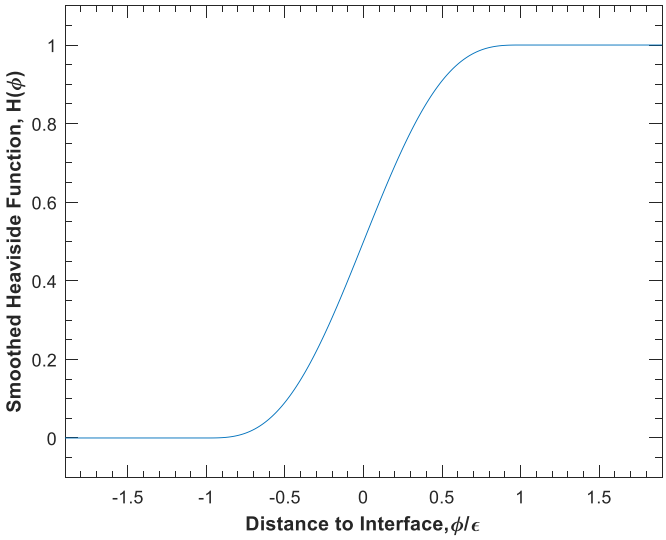

Figure 2. The smoothed Heaviside function used to transition fluid properties. On the left-hand side, where the value of the scalar ϕ is less than -1ϵ, the fluid is treated as a pure gas. On the right-hand side, where value of the scalar ϕ is more than $+1\epsilon$, the fluid is treated as a pure liquid. In between, the properties of the fluid are blended (equation (5)) according to the smoothed Heaviside function.

$$H(\phi) = \left\{ \begin{array}{cc} 0, & \phi < -\epsilon \\ \frac{1}{2}\left[1 + \frac{\phi}{\epsilon} + \frac{1}{\pi}\sin\left(\frac{\pi\phi}{\epsilon}\right)\right], & |\phi| < \epsilon \\ 1, & \phi > \epsilon \end{array} \right\}. \tag{4}$$

This Heaviside function is used to blend fluid properties according to

$$\alpha(\phi) = \alpha_1 H(\phi) + \alpha_2 (1 - H(\phi)) \tag{5}$$

where α represents a generic fluid property, α_1 is the value of that property in a pure liquid and α_2 is the value of that property in a pure gas.

For the property ramp to provide consistent results, the scalar (ϕ) must be a true distance function (i.e. $\nabla\phi = 1$), which is not intrinsically guaranteed using just equation (3). Thus, to maintain the scalar (ϕ) as a distance function, the following equation is iteratively solved in between timesteps:

$$\frac{\partial \phi_d}{\partial \tau} = \text{sign}(\phi)(1 - |\nabla\phi_d|) \tag{6}$$

where ϕ_d is the corrected scalar, τ is the pseudo-time used in re-distancing, ϕ is the scalar that needs to be restored from the advection in equation (3), and sign (ϕ) is given by,

$$\text{sign}(\phi) = \left\{ \begin{array}{cc} -1, & \phi < -\epsilon_d \\ \left[\frac{\phi}{\epsilon_d} + \frac{1}{\pi}\sin\left(\frac{\pi\phi}{\epsilon_d}\right)\right], & |\phi| < \epsilon_d \\ 1, & \phi > \epsilon_d \end{array} \right\} \tag{7}$$

where ϵ_d is the interface half-thickness and can differ from the ϵ used to blend fluid properties in equation (4).

2.2. Plasma hydrodynamics solver—nonPDPSIM

The plasma hydrodynamics model *nonPDPSIM* is a 2D, vertex-centered finite-volume method numerical code executed on a unstructured mesh [31]. The unstructured mesh feature is important for this project in order to properly resolve the boundaries of the bubble and electrodes. The numerical mesh is static with refinement zones to vary the mesh density.

In *nonPDPSIM*, Poisson's equation for the electric potential is solved concurrently with continuity equations for charged and neutral species, and radiation transport. The solution for electric potential and charged species density is obtained implicitly, using adaptive time stepping which is initiated on the order of picoseconds and is then dynamically updated to maximize the efficacy of the solver. While *nonPDPSIM* has the capability to simultaneously solve the compressible Navier–Stokes equation for convective transport of neutral species, the time for evolution of the plasma streamers in the bubble is typically short compared to any convective motion. Therefore, only diffusive transport of neutral species was considered. For the same reasons, net bubble movement or deformation occurs on a significantly longer timescale (hundreds of microseconds to milliseconds) than propagation of the streamer. The shape of the bubble is therefore static during the plasma simulation.

Although *nonPDPSIM* has the capability of resolving plasma transport into condensed phases (such as water), in this work water was represented as a solid lossy dielectric with a specified permittivity and conductivity. This approximation is valid for conditions where the time for streamer propagation (∼several nanoseconds) is short compared to the dielectric relaxation time of the liquid (several microseconds), and short compared to the time required for solvated charged species to diffuse away from the surface of the liquid [17]. Both of these conditions were met in this study.

The algorithms and numerical techniques used in *nonPDPSIM* are described in detail in prior publications [31, 37–40], and so only those relevant to this work will be briefly described here. Poisson's equation was solved for the electric potential,

$$\nabla \cdot (\varepsilon \cdot \nabla \Phi) = -\left(\sum_j q_j \cdot N_j + \rho_{\mathrm{M}} \right) \tag{8}$$

where ε is the electric permittivity, Φ is the electrical potential, q_j is the charge of species j (singly charged ion or electron), N_j is the number density of species j, and ρ_{M} is the charge density in materials and on surfaces. The permittivity varies as a function of position, with values appropriate for the local materials. Simultaneously, continuity equations for charged particle densities are integrated using,

$$\frac{\partial N_j}{\partial t} = -\nabla \cdot \vec{\Gamma_j} + S_j + \left(\sum_m -\nabla \cdot \vec{\Gamma_m} \gamma_m + \sum_k -\nabla \cdot \phi_k \gamma_k \right) \tag{9}$$

where $\vec{\Gamma_j}$ is the flux of species j and S_j is a source term for changes in densities due to collisions, including photoionization and radiation transport [31]. The terms in parentheses are only solved for electrons on plasma boundaries (first sum), or photons of flux ϕ_k with secondary emission coefficient γ_k. Charge density on and in solid materials ρ_{M} is solved for using,

$$\frac{\partial \rho_{\mathrm{M}}}{\partial t} = -\nabla \cdot (\sigma (-\nabla \Phi)) + \left(\sum_j q_j \left(-\nabla \cdot \vec{\Gamma_j} (1 + \gamma_j) \right) + \sum_k \phi_k \gamma_k \right) \tag{10}$$

where σ is the conductivity and the terms in parentheses are only solved for on material surfaces. After the charged particle densities and electric potential have been updated, the electron temperature T_{e} is updated using

$$\frac{\partial \left(\frac{3}{2} n_{\mathrm{e}} k_{\mathrm{B}} T_{\mathrm{e}} \right)}{\partial t} = e \vec{\Gamma_{\mathrm{e}}} \cdot (-\nabla \Phi) - \nabla \cdot \left(\frac{5}{2} k_{\mathrm{B}} T_{\mathrm{e}} \vec{\Gamma_{\mathrm{e}}} - \kappa \nabla T_{\mathrm{e}} \right) - n_{\mathrm{e}} \sum_i \Delta \varepsilon_i k_i N_i \tag{11}$$

where k_{B} is Boltzmann's constant, e is the elementary charge, and κ is the electron thermal conductivity. The final term is summation over electron collisions with species of number density N_i with a rate coefficient k_i causing changes in electron energy $\Delta \varepsilon_i$, where $\varepsilon = \frac{3}{2} k_{\mathrm{B}} T_{\mathrm{e}}$. Electron impact rate and transport coefficients are obtained from stationary solutions of Boltzmann's equation for the electron energy distribution. Radiation transport was addressed using a Green's function propagator technique. Radiation was considered from high lying states of N_2 photoionized O_2 and H_2O with a cross-section of 1×10^{-17} cm^2. To reduce the computational burden of the radiation transport calculation (and reduce memory requirements), radiation transport was only considered for pairs of computational nodes within 0.1 mm of each other.

Information from PHASTA simulations was transferred to *nonPDPSIM* via a four-step one-way process shown in figure 3. (i) Select a 2D snapshot from a PHASTA simulation (figure 3(a)); (ii) visualize the distance field (ϕ) in that 2D plane with a visualization tool (paraview), converting that snapshot to a greyscale image with bubbles in light grey (negative values of ϕ), solid domain in dark grey (non-fluid regions), and liquid in black (positive values of ϕ) (figure 3(b)); (iii) trace and obtain the co-ordinates of the bubble and solid domain shapes (figure 3(c)); (iv) convert the point arrays into a mesh for *nonPDPSIM* (figure 3(d)).

3. Description of the experiment

In our previous work [41], we investigated the physics of bubble formation for a five-nozzle air inflow capillary and the succeeding bubble dynamics. To investigate the process of bubbles colliding into pin-shaped electrodes and for the experimental imaging of discharge in the system, the gas feed capillary was reduced to a single-nozzle arrangement, in which it was much easier to guide and isolate bubbles between the electrode gap. The experimental setup used a pair of pin electrodes placed 50 mm above the air inflow capillary. Further fluid dynamic statistics for the single-nozzle capillary not included

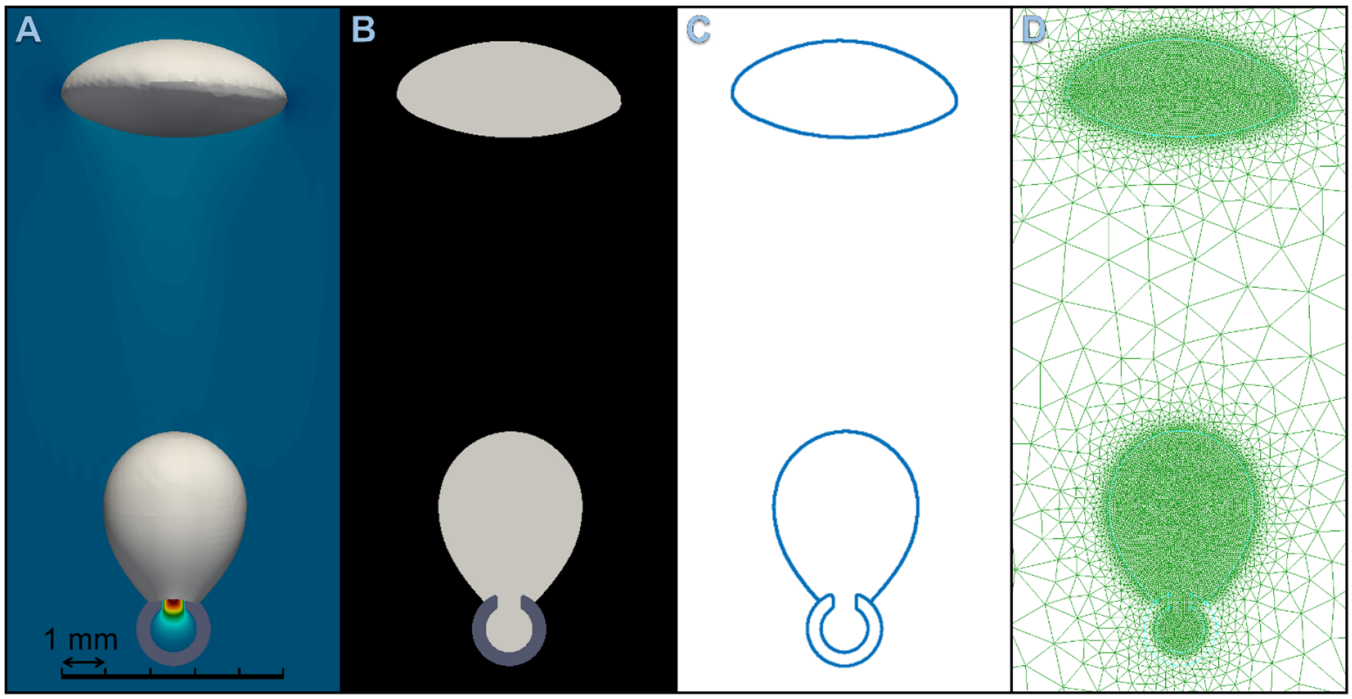

Figure 3. Information transfer from PHASTA to *nonPDPSIM*. (A) PHASTA image. (B) Greyscale slice of PHASTA simulation. (C) Points collected along phase boundary for pointwise mesh. (D) Pointwise mesh.

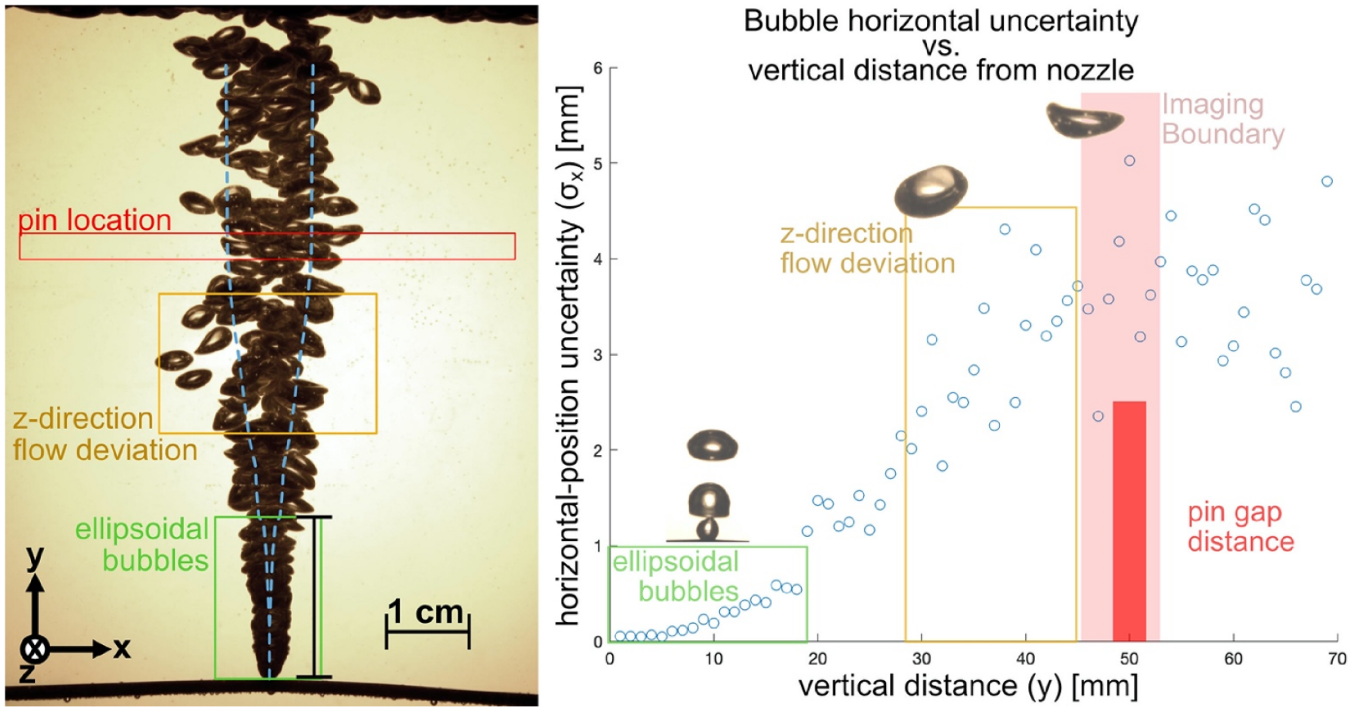

Figure 4. Composite image of 21 bubble flow-path images at 100 ml min^{-1} and corresponding plot of horizontal-position standard deviation (σ_x; blue dotted-line/circles) from injection nozzle position as a function of vertical distance from injection point. Three regimes are highlighted—well-behaved ellipsoidal bubbles (green), serpentine flow-path at which bubbles 'avoid' electrodes (yellow), and deformed bubble regime where pin electrodes are positioned (red). The pink region delineates the boundary of the imaging frame.

in our previous work have been shown in figure 4 to justify the imaging methodology.

The experiment consists of the inflow capillaries positioned at the base of a 500 ml tank of deionized water. Bare copper electrodes (3.2 mm in diameter) are sealed to the side of the tank such that a variable gap is aligned with the flow-path of the injected stream of bubbles. Bubble shape is informed by statistical data gathered experimentally and computationally

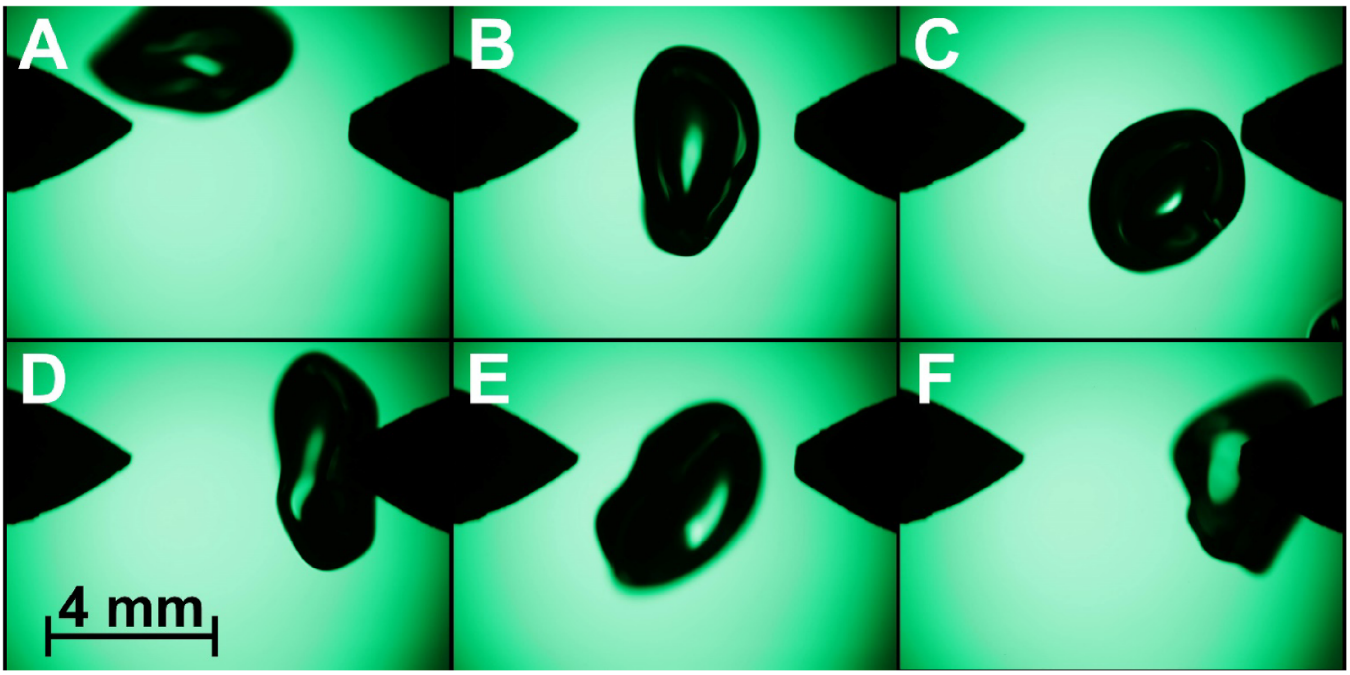

Figure 5. Variation of bubble deformation observed between electrodes at 5 cm distance from the bubble injection point. Blurring of perimeter (A), (F) due to slight z-axis displacement of bubble depth and orientation. Axial orientation can be horizontal (A), vertical (B), or rotated along the y-axis to face the camera (C). Pin/bubble collisions (D) are common.

as a function of shape-by-injection-point distance [42, 43] as carried out in our previous work. Bubble eccentricity is strongly correlated with the bubble distance from injection point (see section 4), while the bubble size is primarily a function of nozzle-size, and secondarily a function of gas flow rate. Bubble deformation is a function of gas flow rate, the distance beyond the injection point, and the proximity to the electrodes (up to point of collision).

Distance from the bubble injection point also correlates with a greater horizontal positional scatter of the bubbles. To determine the likelihood of capturing a bubble positioned near the electrode gap, the standard deviation of horizontal position binned by 1 mm increments is plotted as a function of vertical position from the injection point (figure 4). The bubble flow-path is divided into three regimes: well-behaved reproducible bubbles that have an elliptical cross-section (outlined in green); a regime where deformation begins in which a serpentine flow-path directs bubbles in the z-direction, away from the electrode position temporarily (outlined in yellow); and the regime in which deformed bubbles travel back to a z-position relatively close to the injection point and electrode gap region (outlined in red). At the height of 50 mm the electrodes will likely interact with collisional bubbles, while some bubbles are still observed positioned between the electrode (figure 5). Due to the horizontal deviation (σ_x) at this desired bubble regime, triggering the experiment to capture discharge events for a specific bubble position presents many challenges. The approach to gather a large image-set of backlit bubble boundaries and long exposure imaging was utilized to determine the qualitative behavior of plasma within highly deformed bubbles.

Bubbles in this flow-path regime are observed rotated about the z-axis (figures 5(b) and (e)), about the x-axis (figure 5(c)), or stretched in collision (figure 5(d)). Due to the inconsistencies of shape in this regime repeatability is hindered. However, the boundary interface deformation leading to the local electric field enhancement being computationally investigation can be isolated. The stochastic nature of these conditions limits synchronization of bubble position and discharge event to long exposure times (1 s) to capture the moment when a bubble passes near the electrode gap at the time the pulse generator applies a high-voltage pulse. Bubbles passed within the region-of-interest 50% (200 images) of the time for a set of 397 images, and between the electrode gap 9% (37 images) of the time.

The copper electrodes are powered by a triggered high-voltage pulse generator (Megaimpulse NPG-18/100k) at a 20 Hz repetition frequency, +18 kV peak amplitude with a 4 ns applied voltage rise-time and 9 ns pulse width (FWHM). The bubbles had an average flow rate of 30 bubbles per second, such that the envelope peak of the generator and bubble frequencies has a period of about 100 ms. Combined with the probability of a bubble passing near the electrode gap, discharge in an injected bubble can be expected to occur every second under best case conditions. Long exposure imaging was performed with a digital single-lens reflex camera (Canon EOS 6D) set at 1 s exposure times to capture the overall development of the plasma across a bubble near the electrodes. All streamer and plasma propagation are captured in a single image such that only qualitative comparisons are made with simulation (volumetric vs surface discharge).

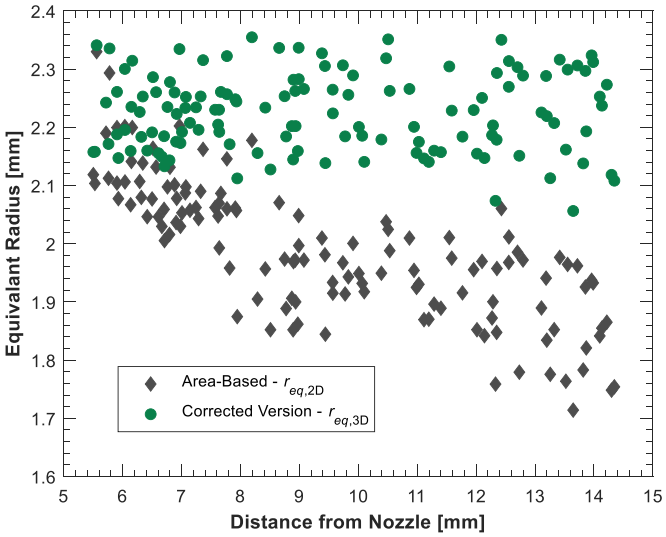

Figure 6. Conventional equivalent radius, $r_{eq,2D}$ (♦) and a corrected version, $r_{eq,3D}$ (●) as a function of the vertical distance the bubbles have traveled.

3.1. Initialization of the fluid dynamics simulations

The initial bubble sizes and positions for bubbles in the simulations were drawn from aggregated experimental images taken with an air inflow rate of 700 ml min^{-1} using a five-nozzle air inflow capillary. The experimental images were cropped and pre-processed to produce the position and area. Ellipses were also fitted to each bubble to provide a value for the major (a) and minor (b) axes. This ellipse fitting and general data calculation procedure has been described in our previous work [41, 42].

The experimental data was then further processed to provide the equivalent radius of each bubble. The equivalent radius of each bubble was calculated in two stages (figure 6). The first stage produces a radius of an equivalent circular bubble ($r_{eq,2D}$) with the same area:

$$r_{eq,2D} = \sqrt[2]{\frac{A}{\pi}}. \tag{12}$$

The second stage corrects this radius with the knowledge that the bubble shape is 3D, and with the assumption that the bubble is an oblate spheroid, i.e. that the value of its third axis (into and out of the plane of the page), c, is the same as the value of the major axis a. The equivalent radius ($r_{eq,3D}$) of a spherical bubble given an oblate spheroid projected onto a 2D plane is given by

$$r_{eq,3D} = r_{eq,2D} * \sqrt[6]{\frac{a}{b}}. \tag{13}$$

The effect of this correction is shown in figure 6, where the corrected equivalent radius does not change as the bubbles rise, but the uncorrected equivalent radius does. As the bubbles deform into ellipsoids, their apparent area on the projected plane decreases, but the true bubble volume does not. Since the camera only captures the area on the projected plane, this correction must be made.

The data for each bubble were sorted into bins based on the number of bubbles between it and the first nozzle and the most likely nozzle the bubble originated from. For the simulations in this work, the final bins took the form of a 3×5 matrix, with one column for each nozzle, and one row for each of the first three departed bubbles from the nozzle (bubbles still attached to the nozzle were flagged separately and discarded). Outliers were discarded, such as bubbles that were too small due to attachment to the nozzles or bubbles that were too large due to early coalescence. This sorting showed that bubbles formed at the first two nozzles were typically larger (and had a tighter size interval) than those formed at the last three nozzles.

The mean and standard deviation were generated for the bubble size and position data in each bin. Rather than using the raw y-position data in the top two bins (i.e. bubbles furthest from the nozzle), the data were generated such that the average bubble-to-bubble distance was conserved. This data was then used to generate pseudorandom initial conditions for the bubbles.

The process for the mesh design was closely aligned with the process outlined in our previous work [41]. The main differences were as follows: (a) the domain dimensions were reduced to match experimental dimensions captured by imaging, (b) a fixed number of bubbles were seeded (14 or 15) and there was no air inflow, and (c) two pin-shaped electrodes were added as obstacles for the bubbles. The mesh was designed such that the bubbles would remain in the refined mesh volume during the entire simulation (with tetrahedral elements of edge length 83.3 μm, as shown between the electrodes in figure 7). Other attributes of the mesh are presented in table 1.

4. Simulation of rising bubbles and streamers

Data pertaining to the bubble shape and size were collected and compared between experiments and simulations to validate the data obtained from the simulations. Since the data collected by PHASTA's bubble tracking algorithm does not include values for major or minor axes of an ellipsoid, those data were extracted from two parameters that are tracked and calculated from the bubbles—the bubble deformability factor, B_{deform}, which is the ratio of the minimum value of the level-set function in the bubble, and the equivalent radius, $r_{eq,3D}$, which is the radius that a spherical bubble of the same volume would have. Using those relations, and the assumption that the bubbles in the simulations are oblate spheroids (which proved to be a good assumption, as shown in figure 6), the major (a) and minor (b) axes of an oblate spheroid were given by

$$a = \frac{r_{eq,3D}}{\sqrt{B_{deform}}} \tag{14}$$

$$b = B_{deform} \times r_{eq,3D}. \tag{15}$$

The evolution of the major (a) and minor (b) axes measured in experiments can then be used to calculate the eccentricity of

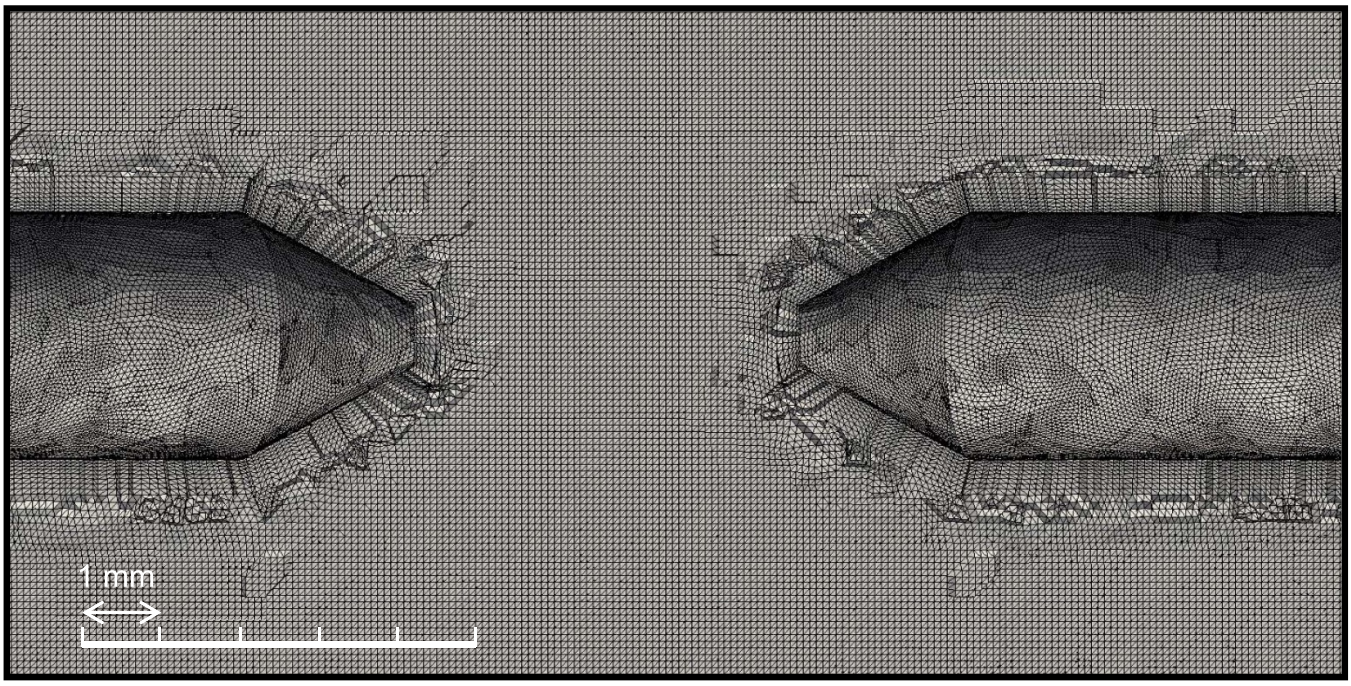

Figure 7. Mesh around the electrodes.

Table 1. Mesh parameters for pin-to-pin cases.

Parameter	Bubbles to electrodes
Total number of mesh elements	682 000 000
Number of parts when split[a]	65 536
Approximate dimensions of well-meshed volume	50 000 μm × 24 000 μm × 10 000 μm
Typical element size	83.3 μm
Starting boundary layer size	10.0 μm
Number of boundary layer elements—nozzle body	8
Total boundary layer size—nozzle Body	457.4 μm
Number of boundary layer elements—nozzle tip	5
Total boundary layer size—nozzle tip	297.7 μm

[a] This is equivalent to the number of CPU cores that the case is run on.

the bubbles, which is a parameter of an ellipse that characterizes its shape,

$$e = \sqrt{1 - b^2/a^2}. \tag{16}$$

A circle has an eccentricity of $e = 0$ and a straight line ($b = 0$) has an eccentricity of $e = 1$.

In both the experiments and simulations, the bubbles start with spherical shapes (i.e. $a = b$). As the bubbles rise, they slowly deform into oblate spheroids. There is a peak eccentricity of about 0.9 observed for both experiments and simulations. After bubbles reach this peak, they start to behave more independently, with some bubbles changing their shape and losing their eccentricity faster than others (figure 8).

4.1. Bubbles chosen for plasma simulations

Three cases were developed utilizing the pin-to-pin geometry with bubble snapshots from an experiment (figure 9) and a simulation (figure 10). In all cases a single bubble was used and considered static due to the nanosecond timescale of the electrodynamics. The first case (figure 9(b)) was based on an experimental image (figure 9(a)), the second was based on a circular bubble (figure 9(c)) with the same equivalent radius as the bubble in the experiments, and the third was based on a snapshot obtained using DNS (figure 10). The domain for these pin-to-pin simulations was shown in figure 1. The simulations were initialized with bubbles filled with humid air (77.2% N_2, 20.8% O_2, 2% H_2O) at 760 Torr and 300 K. The humid-air plasma reaction mechanism is based on the work of van Gaens *et al* [42] and Norberg *et al* [31, 43]. A subset of the full reaction mechanism was used due to the short duration of the current pulses. For example, higher order HNOx species were not included as several reactions over many tens of microseconds to ms are required for these species to be generated. In the first and third cases the initial background electron density was set to 1×10^8 cm^{-3} (with an ion density 5×10^7 cm^{-3} of N_2^+ and O_2^+ to maintain charge neutrality). The second case was seeded with more dense pockets of electrons and ions, although similar behavior was noted in a version with

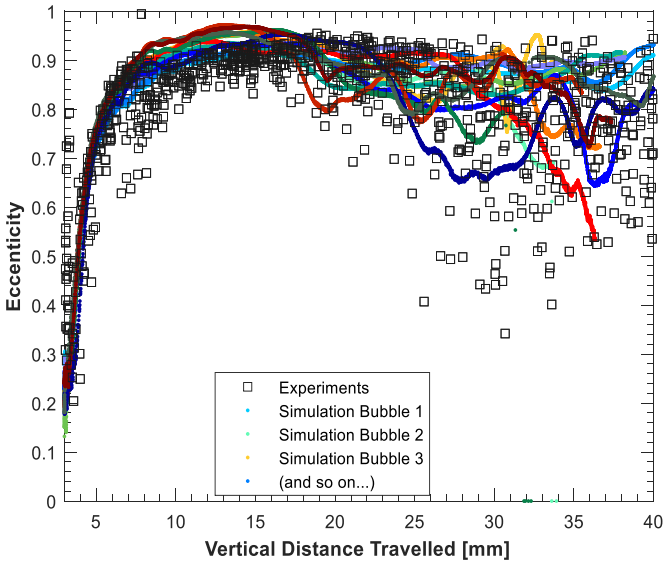

Figure 8. The evolution of bubble eccentricity of bubbles in experiments (□) and simulations (shown as dots). Data for simulations are shown in a unique color for each of fifteen individually tracked bubbles. The air inflow rate for the experimental case was 700 ml min^{-1}, where bubbles were produced out of all five nozzles. The initial conditions for the simulations were seeded using experimental data.

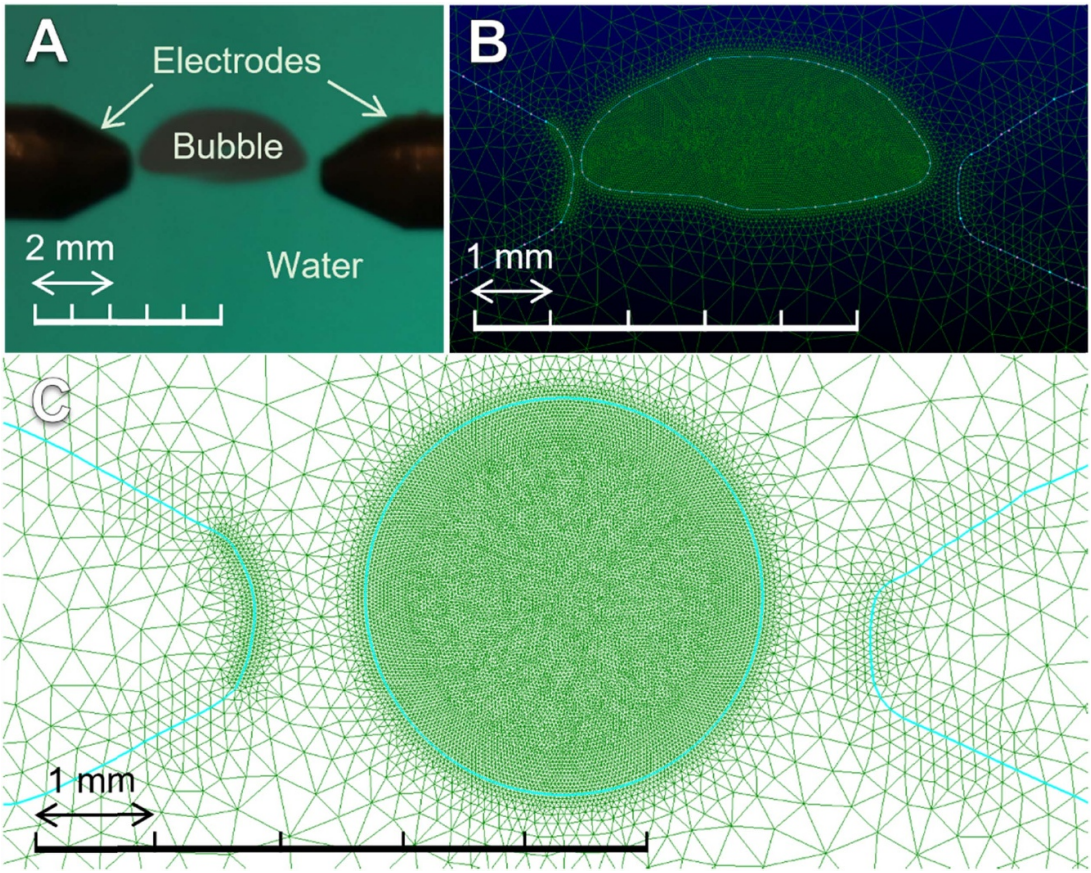

Figure 9. (A) Experimental image of a bubble between two electrodes. (B) A mesh generated using shape data from the image. (C) A mesh generated with the same electrodes as in (A) and (B), with a spherical bubble (10 600 nodes) that has the same equivalent radius as the bubble in Mesh B. The mesh element side length within each bubble is uniform at approximately 6.5 μm.

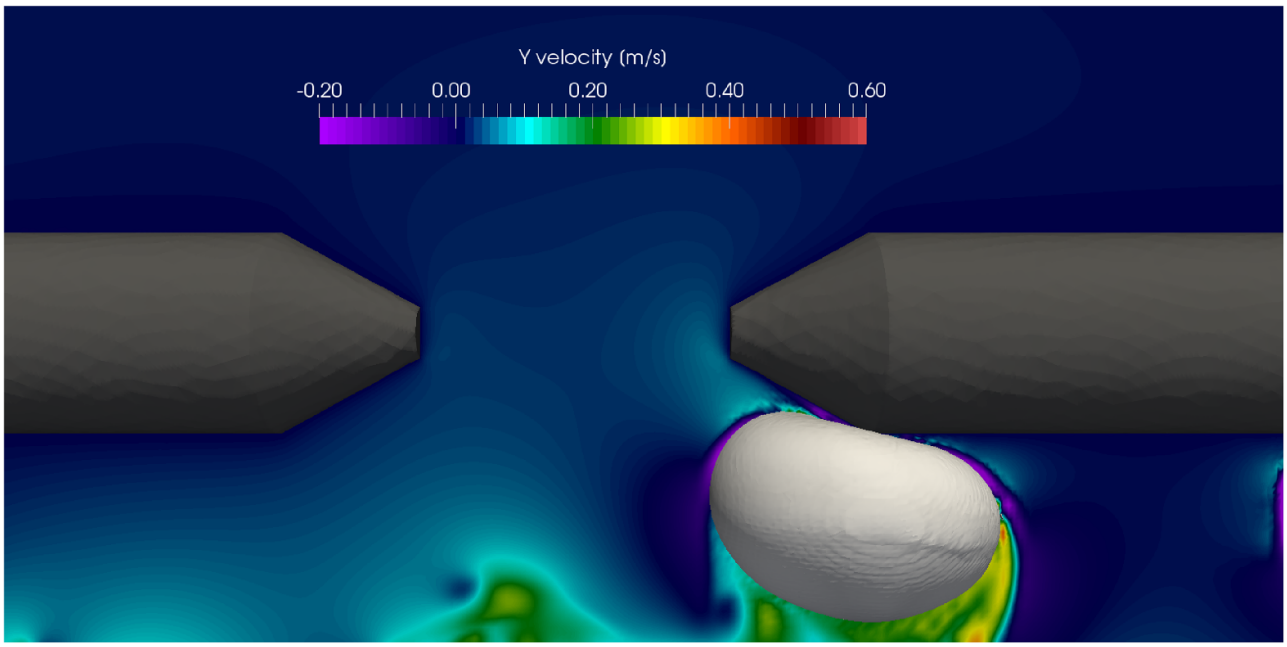

Figure 10. DNS snapshot of a bubble colliding with an electrode.

a preset background electron density. The powered electrode was ramped linearly from 0 to +12 kV over 1 ns and then held at that value for the remainder of each simulation.

The distribution of the electric field in these three cases after the voltage ramp was completed is shown in figure 11. Small portions of each bubble experience an electric field strength over 30 kV cm^{-1} and most of each bubble experiences an electric field greater than 20 kV cm^{-1}. We are mainly interested in the regions with the highest electric field strength, since regions with an electric field strength around 30 kV cm^{-1} tend to undergo electric breakdown which leads to streamer development. In the first and third bubbles, the electric field is greater on one side than the other, while the electric field distribution in the second bubble is more symmetrical (albeit not totally so). The lack of perfect symmetry is likely due to the asymmetry in the shapes of the electrodes. The electric field tends to be larger in the bubble rather than in bounding water as electric fields are typically larger in low permittivity materials than in bounding high permittivity materials. However, the maximum electric field is not necessarily in the bubbles (for this to be the case, the primary applied electric field should go from top to bottom), as refraction of the electric field lines at the air/water interface creates a local enhancement of the electric field. This is most clearly seen in the third image of figure 11, where the refraction of the electric field lines due to the difference in permittivity between water and air results in the extension of a stronger electric field through the water and into the bubble.

4.2. Streamer development

The evolution of electron density in the case with the bubble shape provided by the experimental image (figure 9(a)) is shown in figure 12. The streamer in this case is the fastest of those presented in this paper (travelling at up to 0.3% the speed of light, approximately 1×10^8 cm s^{-1}), while having the highest plasma density compared to streamers in the spherical and deformed bubbles. The peak electron density was 2×10^{17} cm^{-3}, which is an order of magnitude higher than that in the other two bubbles. The electric fields at the head of the streamer reached 210 kV cm^{-1}, corresponding to an *E/N* of 860 Td. The electron temperatures at the head of the streamer reached 4–7 eV. The propagation of the streamer was largely driven by electron impact ionization, the source term for which was above 3×10^{27} cm^{-3} s^{-1} and was typically 1–2 orders of magnitude above the source term for electrons produced from photoionized O_2 (peaking at 7×10^{25} cm^{-3} s^{-1}) which in turn was typically an order of magnitude above the source term for electrons produced from photoionized H_2O (peaking at 8×10^{24} cm^{-3} s^{-1}).

The evolution of electron density for the circular bubble is shown in figure 13. In this simulation, there were two regions of seed charges with a maximum density of 1×10^{-12} cm^{-3} placed at either side of the bubble (see top-left pane of figure 13) as these were the regions with the highest vacuum electric fields. Seed charges were also used in this simulation to more clearly show the effects of the electron avalanches at either side of the bubble (mainly that the avalanche on the left side is far outpaced by that on the right side). So, depending on the physical origin of these seed charges, and whether one or both are present in experiments, the dynamics could be different.

In figure 13, the large electron avalanche starts with the seed charge closer to the grounded electrode, which eventually meets the electrons from the other seed charge and splits off slightly before diffusing and recombining with ions in

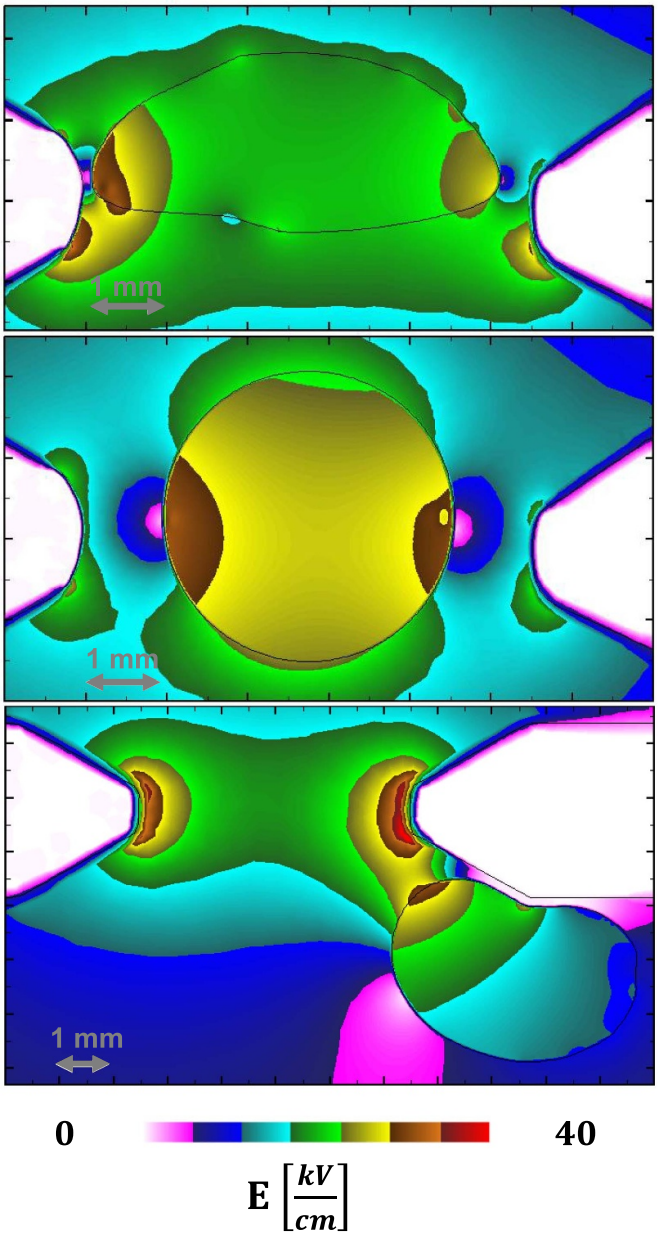

Figure 11. Electric field enhancement in bubbles near pin-shaped electrodes. In each of these simulations, the left pin electrode was powered at +12 kV, and the right pin electrode was grounded. The bubbles in the top two panes are the same as the bubbles in figure 9, and the bubble shape in the lowest pane was obtained from DNS.

the surroundings. During this period (i.e. the first 10 ns of the simulation), ionization is dominated by photoionization effects, and in the first 5 ns, the source term for electron impact ionization is negative in most regions, suggesting that there are more recombination and attachment events than ionization events. Meanwhile, when the first electron avalanche hits the left side of the bubble, two surface ionization waves (SIWs) start to form on the right side of the bubble. One SIW moves towards the top of the bubble, while the other moves towards the bottom, symmetrically. The peak electric field strength in the SIWs was about 90 kV cm^{-1} (370 Td) and the source terms for electrons produced from electron impact ionization was on the same order of that for electrons produced from photoionization, around 2 $\times 10^{25}$ cm^{-3} s^{-1}. The electron temperatures in these streamers were at 3–5 eV.

After the SIWs reach the position demonstrated in the final pane of figure 13, the electron density throughout the bubble starts to subside as the conductive plasma inside the bubble reduces the local E/N, which increases the electric field in the bounding water, and reduces electron temperature. The rate of recombination (7 $\times 10^{24}$ cm^{-3} s^{-1}) and attachment was up to two orders of magnitude higher than the electron impact ionization rate in adjacent areas (2 $\times 10^{22}$ cm^{-3} s^{-1}), and the electrons are mainly being held

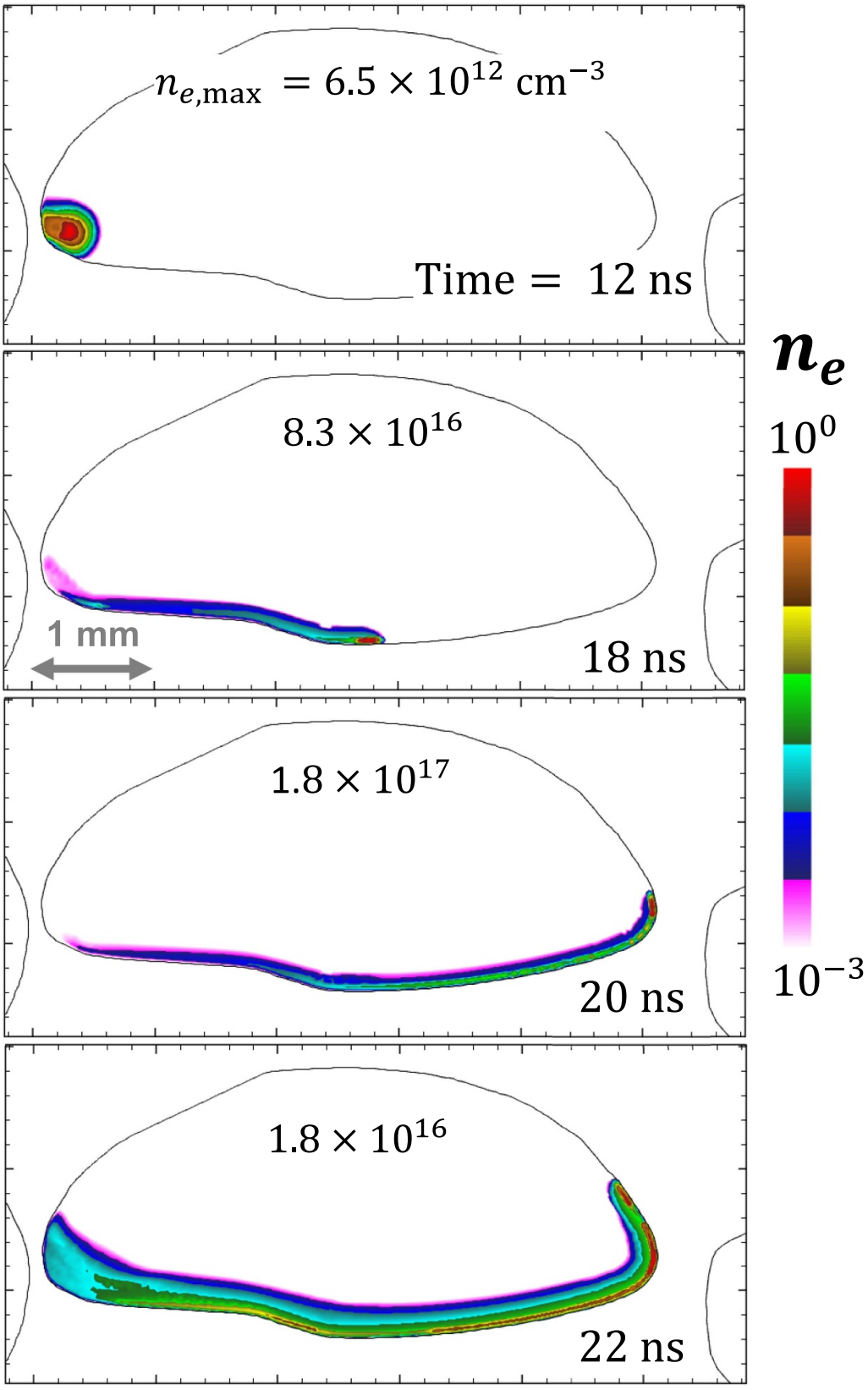

Figure 12. Evolution of electron density (three decade log plot) in a bubble between two electrodes. The electrode was charged at +12 kV (ramped up from 0 linearly over 1.0 ns). The maximum electron density is shown at the top of each pane (in cm^{-3}), and the simulation time is shown at the bottom right of each pane.

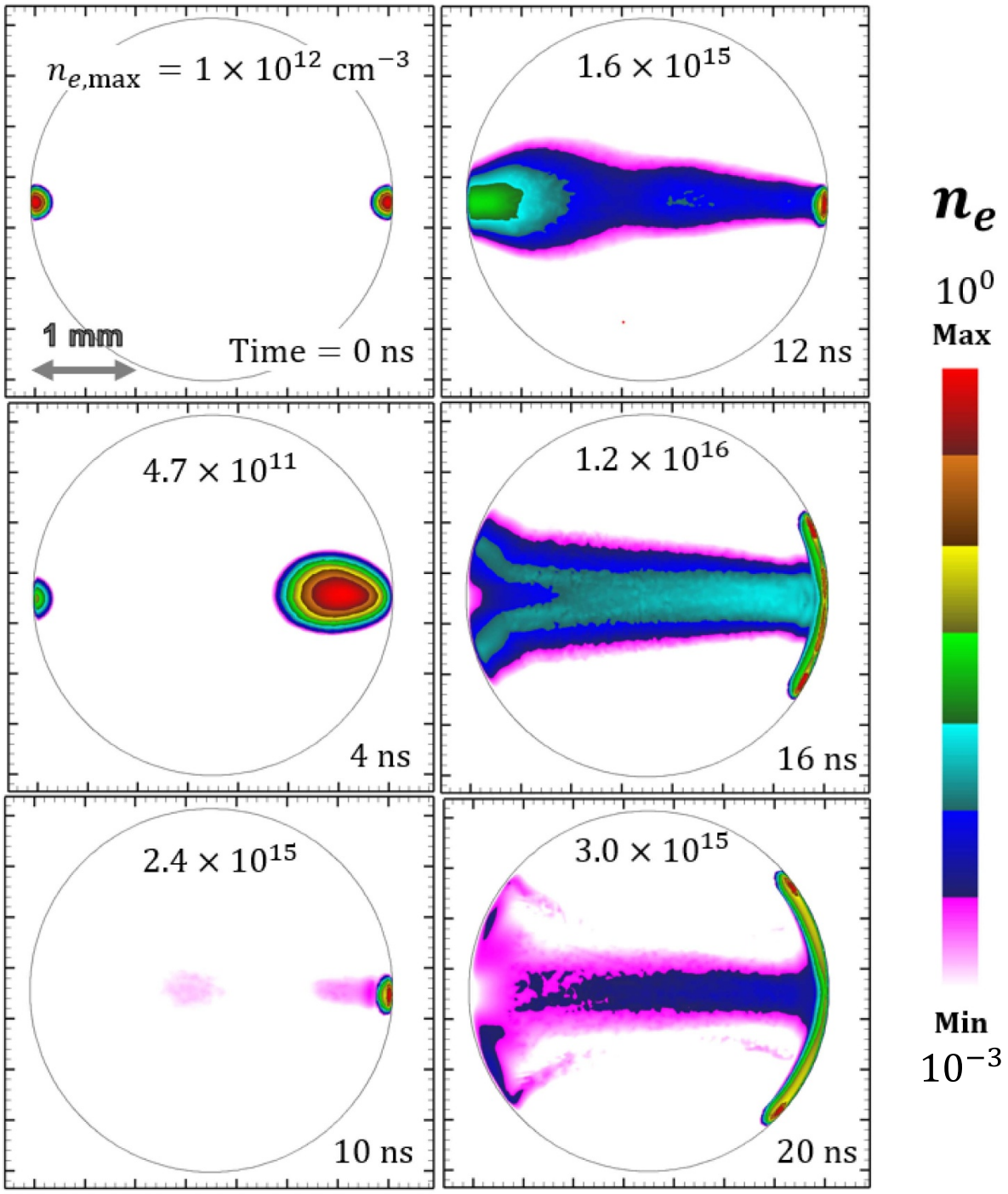

Figure 13. Evolution of electron density (three decade log plot) in a circular bubble between two electrodes. Two seed charges were initially present (top-left pane). The powered electrode (outside of each pane, to the left) was charged at +12 kV (ramped up from 0 linearly over 1.0 ns). The maximum electron density is shown at the top of each pane (in cm^{-3}), and the simulation time is shown at the bottom right of each pane.

in check by the slowly declining rate of photoionization (<3 $\times 10^{24}$ cm^{-3} s^{-1}).

While we were able to experimentally capture an image of a bubble between the two pin electrodes, it is difficult to time the passing of bubbles between the electrodes and the voltage pulses. Furthermore, many bubbles in the fluid dynamics simulations collided with the sides of the electrodes, rather than passing between the pins. This is due to the randomness in the flow path depicted in figure 4, which is also seen in the simulations. Nonetheless, we were able to capture the collision of a bubble with the front of a pin electrode using DNS (figure 10). The simulated evolution of electron density in that bubble is shown in figure 14. The electron avalanche first propagates towards the grounded electrode before two SIWs

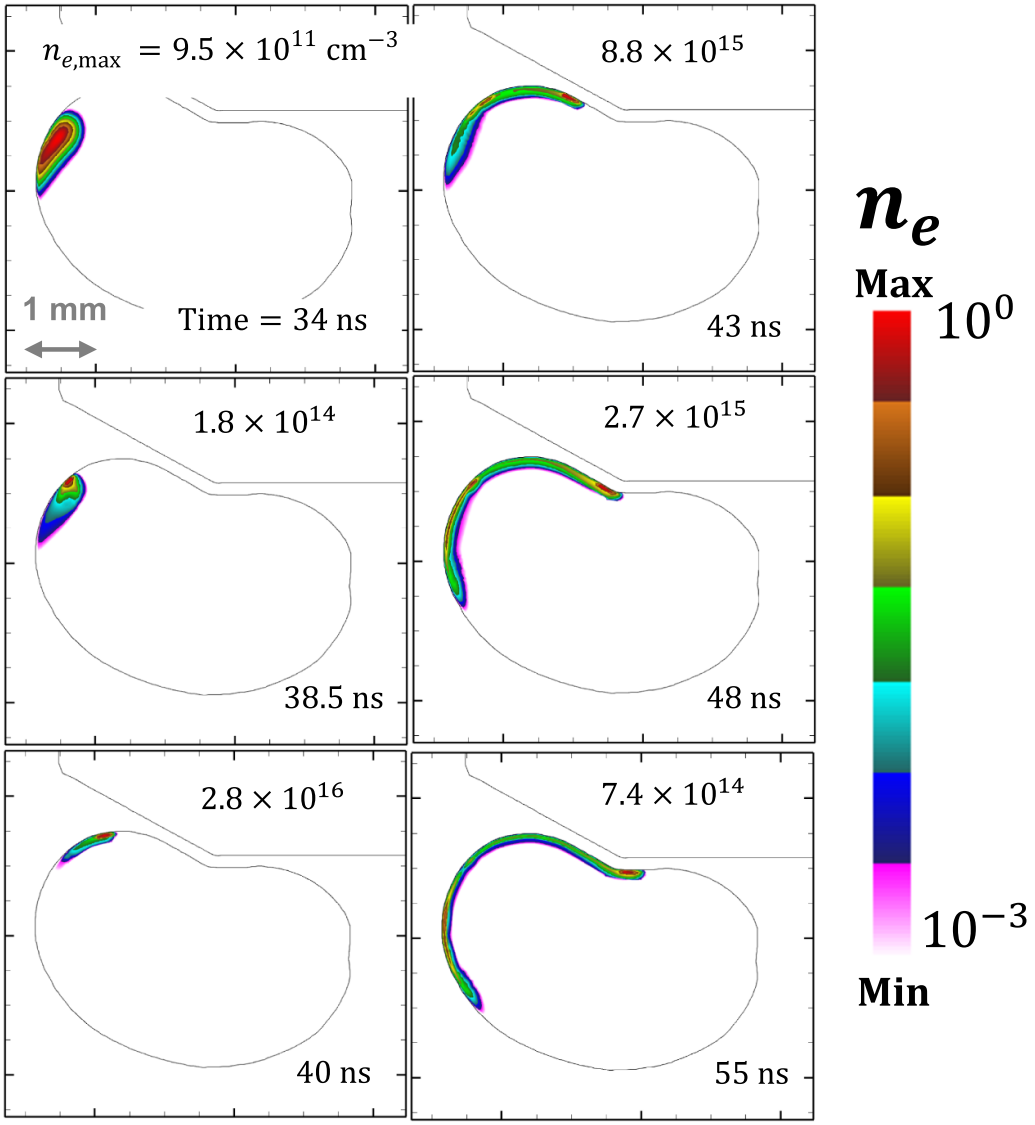

Figure 14. Evolution of electron density (three decade log plot) in a bubble impressed against a pin electrode. The electrode was charged at +12 kV (ramped up from 0 linearly over 1.0 ns). The maximum electron density is shown at the top of each pane (in cm^{-3}), and the simulation time is shown at the bottom right of each pane.

continue from the point of impact of the electron avalanche on the other side of the bubble. The electron temperature at the head of the SIWs is 2–4 eV with electric fields peaking at about 100 kV cm^{-1} (410 Td). Ionization rates peaked at around 1×10^{26} cm^{-3} s^{-1} for electron impact ionization and 1×10^{25} cm^{-3} s^{-1} for photoionization.

4.3. Experimental observations

Long exposure images taken experimentally show clear signs of interface-boundary-bounded streamers that outline the edge of the bubble. Figure 15(a) shows a high contrast boundary at the bottom of the bubble in which deformation is similar to the bubble shape in figure 5(a), with the exception of the portion colliding with the electrode. Above the brightest spot in figure 15(a), a sharply delineated shadow suggests that a portion of the bubble may be wrapping around the electrode. The diffuse light above the surface streamer is likely due to depth-of-field blurring similar to the bubble in figure 5(f). Figure 15(b) demonstrates stronger surface streamers across the bubble boundary above the electrode. In this case, there is little diffuse light within the bubble and multiple streamers outline the bubble. These bubble-outlining emissions correspond with the interface bounded streamer propagation simulated computationally. Though some diffuse emissions may be seen, in both cases, light adjacent to some surface dominate—beginning at the electrode (brightest emission) and traced to the furthest extent of the bubbles-boundary, then finally following the boundary of the bubble back around its curvature away from the electrode, as suggested by figure 12.

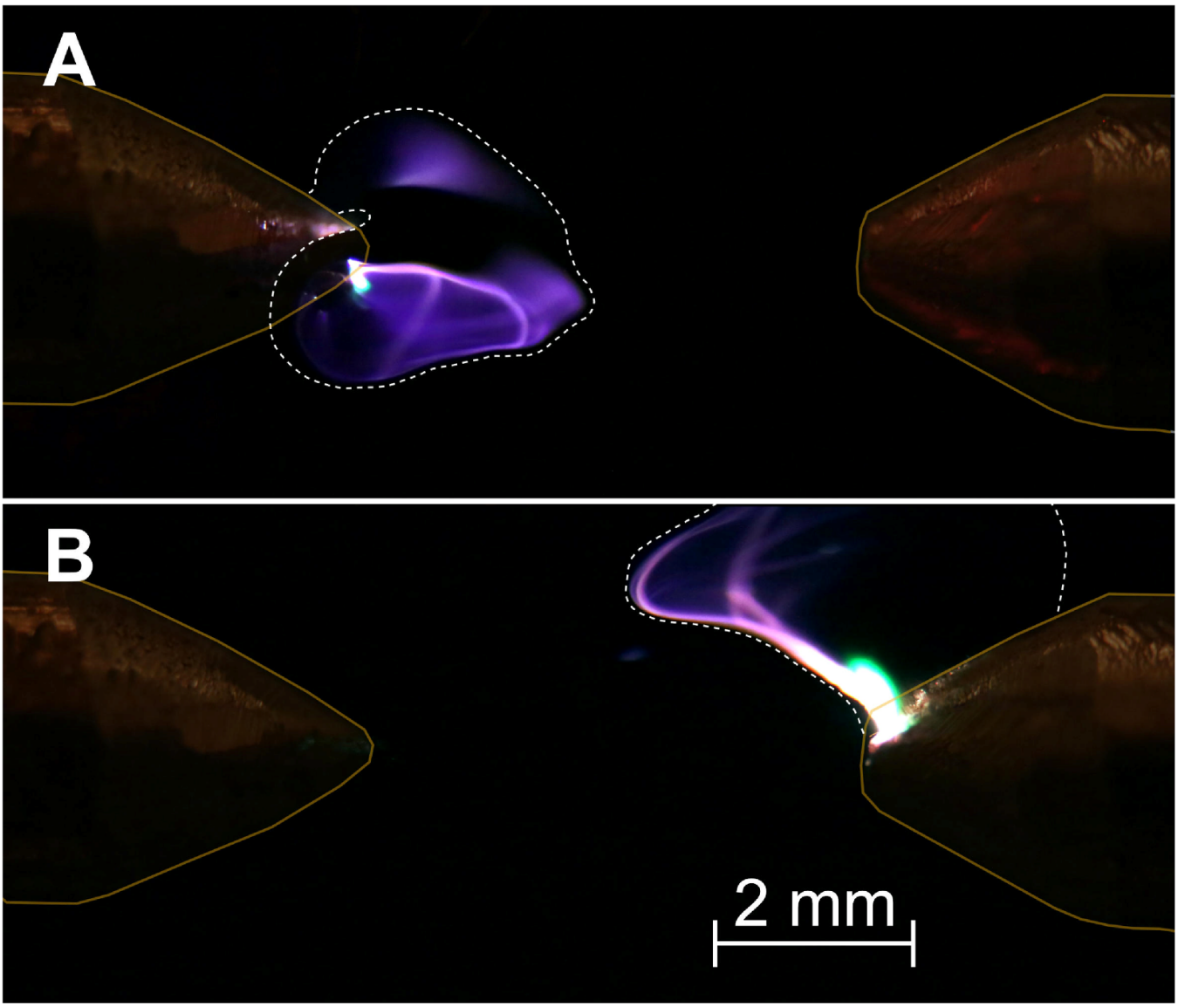

Figure 15. Imaging of discharge from bubble/electrode collision. A bright streamer outlines the edge of bubbles that collide with either the left (A) or right (B) electrode. Blurring in the top pane indicates a portion of bubble that is out of the field of depth along the z-axis. Dotted lines represent the inferred bubble interface.

5. Conclusions

Plasma hydrodynamics simulations have been conducted to investigate streamer propagation in three different bubble shapes: (a) an elliptical profile obtained from an experimental image; (b) an idealized circular bubble with the same equivalent radius and position; (c) a bubble pressed against an electrode with the same equivalent radius tracked through DNS. The simulations showed two different modes for streamer formation in the pin-to-pin setup, depending on the bubble shape. In the elliptical bubble, a short electron avalanche triggered a SIW close to the origin of the avalanche, and thus the vast majority of the plasma propagated along the surface of the bubble (figure 12). In the circular bubble, an electron avalanche first traveled through the middle of the bubble before two SIWs began to propagate from the point closest to the grounded electrode (figure 13) where the volumetric streamer intersected the surface. The results from the simulation in the bubble from DNS, deformed by proximity to an electrode (figure 14) more closely match with that seen in the elliptical bubble. Experiments with a pin-to-pin electrode geometry show good agreement with the behavior predicted by simulations, with streamers appearing to travel on the surface of deformed bubbles (figure 15). The transfer of plasma generated RONS from gas to a liquid bulk require solvation at this phase boundary. Plasma generation supported by the local field enhancement of the deformed bubble surface boundaries is a mechanism that is likely responsible for initiating streamer formation.

Data availability statement

The data that support the findings of this study are available upon reasonable request from the authors.

Acknowledgments

This material is partly based upon work supported by the National Science Foundation under Grant No. PHY 2107901, partly based upon work supported under a Department of Energy Nuclear Energy University Programs Graduate Fellowship. The authors acknowledge Altair Engineering, Inc. for their provision of the Acusim linear algebra solution library, and Simmetrix, Inc. for the libraries provided for mesh-building and domain modeling. We would like to acknowledge Dr Juliusz Kruszelnicki for his instruction and guidance of the code *nonPDPSIM*. The Argonne Leadership Computing Facility (ALCF) has provided us with supercomputer access through the ASCR Leadership Computing Challenge (ALCC) program, which has allowed us to obtain some of the DNS results in this work. The authors gratefully acknowledge support from North Carolina State University's Game-Changing Research Incentive Program for Plant Sciences Initiative (GRIP4PSI). The work of M Kushner was supported by the Department of Energy, Office of Science, Office of Fusion Energy Sciences under Award No. DE-SC0020232 and the National Science Foundation (Nos. PHY-1902878 and IIP-1747739).

ORCID iDs

J T Mast https://orcid.org/0000-0003-0748-2754
Mark J Kushner https://orcid.org/0000-0001-7437-8573
Katharina Stapelmann https://orcid.org/0000-0002-2116-2661

References

[1] Kaushik N K *et al* 2018 Biological and medical applications of plasma-activated media, water and solutions *Biol. Chem.* **400** 39–62
[2] Ranieri P, Sponsel N, Kizer J, Rojas-Pierce M, Hernández R, Gatiboni L, Grunden A and Stapelmann K 2021 Plasma agriculture: review from the perspective of the plant and its ecosystem *Plasma Process. Polym.* **18** 2000162
[3] Foster J E 2017 Plasma-based water purification: challenges and prospects for the future *Phys. Plasmas* **24** 055501
[4] Tachibana K and Nakamura T 2019 Comparative study of discharge schemes for production rates and ratios of reactive oxygen and nitrogen species in plasma activated water *J. Phys. D: Appl. Phys.* **52** 385202
[5] Babaeva N Y, Naidis G V, Tereshonok D V and Smirnov B M 2017 Streamer breakdown in elongated, compressed and tilted bubbles immersed in water *J. Phys. D: Appl. Phys.* **50** 364001
[6] Shigeta M 2013 Three-dimensional flow dynamics of an argon RF plasma with DC jet assistance: a numerical study *J. Phys. D: Appl. Phys.* **46** 015401
[7] Trelles J P, Chazelas C, Vardelle A and Heberlein J V R 2009 Arc plasma torch modeling *J. Therm. Spray Technol.* **18** 728–52
[8] Zhou Q, Li H, Xu X, Liu F, Guo S, Chang X, Guo W and Xu P 2009 Comparative study of turbulence models on highly constricted plasma cutting arc *J. Phys. D: Appl. Phys.* **42** 015210
[9] Trelles J P 2018 Advances and challenges in computational fluid dynamics of atmospheric pressure plasmas *Plasma Sources Sci. Technol.* **27** 093001
[10] Shigeta M 2016 Turbulence modelling of thermal plasma flows *J. Phys. D: Appl. Phys.* **49** 493001
[11] Murphy A B, Tanaka M, Yamamoto K, Tashiro S, Sato T and Lowke J J 2009 Modelling of thermal plasmas for arc welding: the role of the shielding gas properties and of metal vapour *J. Phys. D: Appl. Phys.* **42** 194006
[12] Lindsay A D, Graves D B and Shannon S C 2016 Fully coupled simulation of the plasma liquid interface and interfacial coefficient effects *J. Phys. D: Appl. Phys.* **49** 235204
[13] Tian W and Kushner M J 2014 Atmospheric pressure dielectric barrier discharges interacting with liquid covered tissue *J. Phys. D: Appl. Phys.* **47** 165201
[14] Norberg S A, Tian W, Johnsen E and Kushner M J 2014 Atmospheric pressure plasma jets interacting with liquid covered tissue: touching and not-touching the liquid *J. Phys. D: Appl. Phys.* **47** 475203
[15] Norberg S A, Parsey G M, Lietz A M, Johnsen E and Kushner M J 2019 Atmospheric pressure plasma jets onto a reactive water layer over tissue: pulse repetition rate as a control mechanism *J. Phys. D: Appl. Phys.* **52** 015201
[16] Tian W and Kushner M J 2015 Long-term effects of multiply pulsed dielectric barrier discharges in air on thin water layers over tissue: stationary and random streamers *J. Phys. D: Appl. Phys.* **48** 494002
[17] Kruszelnicki J, Lietz A M and Kushner M J 2019 Atmospheric pressure plasma activation of water droplets *J. Phys. D: Appl. Phys.* **52** 355207
[18] Kolobov V I and Arslanbekov R R 2012 Towards adaptive kinetic-fluid simulations of weakly ionized plasmas *J. Comput. Phys.* **231** 839–69
[19] Tanaka Y 2009 Thermally and chemically non-equilibrium modelling of Ar–N_2–H_2 inductively coupled plasmas at reduced pressure *Thin Solid Films* **518** 936–42
[20] Kushner M J 2009 Hybrid modelling of low temperature plasmas for fundamental investigations and equipment design *J. Phys. D: Appl. Phys.* **42** 194013
[21] Pushkarova R A and Horn R G 2008 Bubble-solid interactions in water and electrolyte solutions *Langmuir* **24** 8726–34
[22] Krasowska M, Malysa K and Beattie D A 2019 Recent advances in studies of bubble–solid interactions and wetting film stability *Curr. Opin. Colloid Interface Sci.* **44** 48–58
[23] Krasowska M and Malysa K 2007 Kinetics of bubble collision and attachment to hydrophobic solids: i. Effect of surface roughness *Int. J. Miner. Process.* **81** 205–16
[24] Zawala J, Kosior D, Dabros T and Malysa K 2016 Influence of bubble surface fluidity on collision kinetics and attachment to hydrophobic solids *Colloids Surf.* A **505** 47–55
[25] Dai Z, Fornasiero D and Ralston J 2000 Particle-bubble collision models—a review *Adv. Colloid Interface Sci.* **85** 231–56
[26] Alizadeh M, Seyyedi S M, Taeibi Rahni M and Ganji D D 2017 Three-dimensional numerical simulation of rising bubbles in the presence of cylindrical obstacles, using lattice Boltzmann method *J. Mol. Liq.* **236** 151–61
[27] Chen G Q, Huang X, Zhang A M, Wang S P and Li T 2019 Three-dimensional simulation of a rising bubble in the presence of spherical obstacles by the immersed boundary-lattice Boltzmann method *Phys. Fluids* **31** 097104
[28] Sponsel N L, Gershman S, Quesada M J H, Mast J T and Stapelmann K 2022 Electric discharge initiation in water with gas bubbles: a timescale approach *J. Vac. Sci. Technol. A* **40** 063002

[29] Jansen K E 1999 A stabilized finite element method for computing turbulence *Comput. Methods Appl. Mech. Eng.* **174** 299–317
[30] Whiting C H and Jansen K E 2001 A stabilized finite element method for the incompressible Navier-Stokes equations using a hierarchical basis *Int. J. Numer. Methods Fluids* **35** 93–116
[31] Norberg S A, Johnsen E and Kushner M J 2015 Formation of reactive oxygen and nitrogen species by repetitive negatively pulsed helium atmospheric pressure plasma jets propagating into humid air *Plasma Sources Sci. Technol.* **24** 035026
[32] Jansen K E 1993 Unstructured grid large eddy simulations of wall bounded flows *Annual Research Briefs* 19940019678 (Center for Turbulence Research) (available at: https://ntrs.nasa.gov/citations/19940019678)
[33] Sussman M, Almgren A S, Bell J B, Colella P, Howell L H and Welcome M L 1999 An adaptive level set approach for incompressible two-phase flows *J. Comput. Phys.* **148** 81–124
[34] Sethian J A 1999 *Level Set Methods and Fast Marching Methods: Evolving Interfaces in Computational Geometry, Fluid Mechanics, Computer Vision, and Materials Science* 2nd edn (Cambridge: Cambridge University Press)
[35] Fang J 2016 Development of advanced analysis toolkit for turbulent bubbly flow simulations *PhD Thesis* North Carolina State University
[36] Brackbill J U, Kothe D B and Zemach C 1992 A continuum method for modeling surface tension *J. Comput. Phys.* **100** 335–54
[37] Babaeva N Y and Kushner M J 2009 Structure of positive streamers inside gaseous bubbles immersed in liquids *J. Phys. D: Appl. Phys.* **42** 132003
[38] Babaeva N Y, Tereshonok D V and Naidis G V 2015 Initiation of breakdown in bubbles immersed in liquids: pre-existed charges versus bubble size *J. Phys. D: Appl. Phys.* **48** 355201
[39] Babaeva N Y and Kushner M J 2008 Streamer branching: the role of inhomogeneities and bubbles *IEEE Trans. Plasma Sci.* **36** 892–3
[40] Babaeva N Y, Bhoj A N and Kushner M J 2006 Streamer dynamics in gases containing dust particles *Plasma Sources Sci. Technol.* **15** 591–602
[41] Pillai N, Sponsel N L, Stapelmann K and Bolotnov I A 2022 Direct numerical simulation of bubble formation through a submerged "flute" with experimental validation *J. Fluids Eng.* **144** 021404
[42] van Gaens W and Boagerts A 2014 Reaction pathways of biomedically active species in an Ar plasma jet *Plasma Sources Sci. Technol.* **23** 035015
[43] Norberg S A 2015 Modeling atmospheric pressure plasma jets: plasma dynamics, interaction with dielectric surfaces, liquid layers and cells *PhD Thesis* University of Michigan